Chemical Science

ROYAL SOCIETY OF CHEMISTRY

EDGE ARTICLE

View Article Online
View Journal | View Issue

Cite this: *Chem. Sci.*, 2024, **15**, 14746

All publication charges for this article have been paid for by the Royal Society of Chemistry

Ultrafast photophysics of *para*-substituted 2,5-bis(arylethynyl) rhodacyclopentadienes: thermally activated intersystem crossing†

Zilong Guo,[b] Yaxin Wang,[b] Julia Heitmüller,[a] Carolin Sieck,[c] Andreas Prüfer,[d] Philipp Ralle,[d] Andreas Steffen,[d] Petr Henke,[eg] Peter R. Ogilby,*[e] Todd B. Marder,*[cf] Xiaonan Ma*[ba] and Tobias Brixner*[af]

Received 30th June 2024
Accepted 14th August 2024

DOI: 10.1039/d4sc04306e

rsc.li/chemical-science

2,5-Bis(phenylethynyl) rhodacyclopentadienes (RCPDs), as a type of Rh(III) complex, exhibit unusually intense fluorescence and slow intersystem crossing (ISC) due to weak metal–ligand interactions. However, details on their ultrafast photophysics and ISC dynamics are limited. In this work, electronic relaxation upon photoexcitation of two substituted RCPDs with two $-CO_2Me$ (A-RC-A) or $-NMe_2$/$-CO_2Me$ (D-RC-A) end groups are comprehensively investigated using femtosecond transient absorption spectroscopy and theoretical analysis. Upon ultraviolet and visible excitation, dephasing of vibrational coherence, charge transfer, conformation relaxation, and ISC are observed experimentally. By calculating the spin–orbit coupling, reorganization energy, and adiabatic energy gap of plausible ISC channels, semi-classical Marcus theory revealed the dominance of thermally activated ISC ($S_1 \rightarrow T_2$) for both D-RC-A and A-RC-A, while $S_1 \rightarrow T_1$ channels are largely blocked due to high ISC barriers. With weak spin–orbit coupling, such differences in plausible ISC channels are predominately tuned by energetic parameters. Singlet oxygen sensitization studies of A-RC-A provide additional insight into the excited-state behavior of this complex.

Introduction

Organometallic complexes have attracted attention for a wide range of applications in photocatalysis,[1–5] bioimaging,[6–8] sensing,[9,10] and organic light-emitting diode (OLED) devices.[11–14] The spin-forbidden nature of the singlet–triplet transition often leads to slow intersystem crossing (ISC) in organic systems. However, by incorporating heavy transition metals, the ISC rate constant (k_{ISC}) can be significantly increased to typically greater than 10^{10} s^{-1},[15] even up to 10^{13}–10^{14} s^{-1} in Ru(II) complexes,[16–19] leading to significant fluorescence quenching and enhanced phosphorescence emission. Efficient ISC can be primarily attributed to strong spin–orbit coupling (SOC) due to participation of the d-orbitals of heavy metals, which can significantly alter the photophysics due to strong metal–ligand interactions *via* metal-to-ligand charge transfer (MLCT) states that dominate electronic relaxation.[20–24]

Unlike complexes with ultrafast ISC, 2,5-bis(phenylethynyl) rhodacyclopentadienes (RCPDs)[25–27] incorporating Rh(III) exhibit up to 69% fluorescence quantum yields (Φ_f) with $k_{ISC} = 10^7$–10^8 s^{-1} which is several orders of magnitude slower than that in Ru(II) complexes.[17] Intriguingly, by replacing Rh(III) with much heavier Ir(III), the corresponding iridacyclopentadienes[28] are still highly fluorescent. Such photophysics was attributed to weakened SOC due to low d-orbital participation in the frontier orbitals and an enlarged S_1–T_1 energy gap (ΔE_{ST}).[28,29] Meanwhile, the T_2 state was reported to be an ISC destination through a thermally activated mechanism in RCPDs,[28] which increased the complexity of their electronic relaxation. Investigations indicated that the fluorescence properties of RCPDs can be effectively tuned by introducing an electron donor (D) or acceptor (A) at the *para*-positions of the arylethynyl groups.[28,30,31] In particular, symmetric substitution with A/A groups ($-CO_2Me$ or $-BMes_2$) (Mes = mesityl = 2,4,6-$Me_3C_6H_2$) at the *para*-positions leads to significantly higher Φ_f than corresponding D/A ($-NMe_2$/$-CO_2Me$) and unsubstituted RCPDs (see Table S1†). In a simple excited-state model, enhanced

[a]*Institut für Physikalische und Theoretische Chemie, Julius-Maximilians-Universität Würzburg, Am Hubland, 97074 Würzburg, Germany. E-mail: tobias.brixner@uni-wuerzburg.de*

[b]*Institute of Molecular Plus, Tianjin University, Tianjin 300072, P. R. China. E-mail: xiaonanma@tju.edu.cn*

[c]*Institut für Anorganische Chemie, Julius-Maximilians-Universität Würzburg, Am Hubland, 97074 Würzburg, Germany. E-mail: todd.marder@uni-wuerzburg.de*

[d]*Department of Chemistry and Chemical Biology, TU Dortmund University, Otto-Hahn-Str. 6, 44227 Dortmund, Germany*

[e]*Department of Chemistry, Aarhus University, Aarhus DK-8000, Denmark. E-mail: progilby@chem.au.dk*

[f]*Institute for Sustainable Chemistry and Catalysis with Boron (ICB), Julius-Maximilians-Universität Würzburg, Am Hubland, 97074 Würzburg, Germany*

[g]*Faculty of Science, Charles University, Hlavova 2030, 128 43 Prague 2, Czech Republic*

† Electronic supplementary information (ESI) available. See DOI: https://doi.org/10.1039/d4sc04306e

fluorescence emission can be attributed either to slow non-radiative relaxation of the S_1 state *via* dark states or suppressed ISC to the triplet state.[32,33] Although k_{ISC} of RCPDs was determined to be 10^7–10^8 s^{-1} using picosecond time-resolved infrared spectroscopy,[30] a full picture of their S_1 relaxation remains unclear. Therefore, a comprehensive picture of the photophysics of RCPDs with weak metal–ligand interactions might be helpful for future rational design of fluorescent emitters.

In general, the ISC rate constant k_{ISC} between singlet (S_m, $m \geq 1$) and triplet (T_n, $n \geq 1$) excited states can be expressed *via* the Fermi golden rule,[34,35]

$$k_{ISC} = \frac{2\pi}{\hbar}\left\langle S_m|\hat{H}_{SO}|T_n\right\rangle^2 \rho_{FC}, \quad (1)$$

in which k_{ISC} is determined by the SOC matrix element $\langle S_m|\hat{H}_{SO}|T_n\rangle$, as well as the Franck–Condon-weighted density of states ρ_{FC}, which can be described in the framework of Marcus–Levich–Jortner theory:[36–39]

$$\rho_{FC} = \frac{1}{\sqrt{4\pi\Gamma k_B T}}\sum_{n=0}^{\infty}\exp(-S)\frac{S^n}{n!}\times\exp\left[-\frac{(\Delta E_{ST}+n\hbar\omega_{eff}+\Gamma)^2}{4\Gamma k_B T}\right].$$

In a semi-classical approximation at high temperature T, with $\hbar\omega_{eff} \ll k_B T$, the Huang–Rhys factor (S) and effective frequency (ω_{eff}) of internal vibrational modes can be ignored. The density ρ_{FC} follows the standard Arrhenius-type equation and k_{ISC} can be obtained from the Marcus-theory equation:[40–43]

$$k_{ISC} = \frac{1}{\hbar}\left\langle S_m|\hat{H}_{SO}|T_n\right\rangle^2\sqrt{\frac{\pi}{\Gamma k_B T}}\exp\left[-\frac{(\Gamma+\Delta E_{ST})^2}{4\Gamma k_B T}\right]. \quad (3)$$

Here, $\langle S_m|\hat{H}_{SO}|T_n\rangle$ describes the SOC matrix element,[44,45] while Γ and ΔE_{ST} represent the reorganization energy and adiabatic energy gap of the ISC ($S_m \rightarrow T_n$, m, $n \geq 1$) transition, respectively. Eqn (3) has been widely employed for estimating ISC and reverse ISC rates in medium-size organic molecules and complexes.[46–49]

In cases of ultrafast ISC ($k_{ISC} > 10^{12}$ s^{-1}) of complexes with late transition metals, extremely high k_{ISC} is observed due to a large coupling term $\langle S_m|\hat{H}_{SO}|T_n\rangle$ up to several thousands of cm^{-1}, which greatly amplifies the ISC rate associated with the ISC barrier (E_a) determined by Γ and ΔE_{ST}. However, RCPDs exhibit much slower ISC ($k_{ISC} = 10^8$–10^9 s^{-1}) due to the lack of strong metal–ligand interactions,[30] *i.e.*, $\langle S_m|\hat{H}_{SO}|T_n\rangle$ in eqn (3) is expected to be small and relatively sensitive to *para*-substitution on the aryl ligand. It is hypothesized that the k_{ISC} may vary significantly with the reorganization energy and adiabatic energy gap subject to para-substitution, which determine the ISC barrier (E_a) thermodynamically and can be discussed within the framework of Marcus theory.

In this work, two *para*-substituted 2,5- bis(arylethynyl)rhodacyclopentadiene complexes (Scheme 1) were investigated by using excitation-wavelength-(λ_{ex}-)dependent femtosecond transient absorption (fs-TA) measurements and time-dependent density-functional theory (TD-DFT) calculations. Compared with A-RC-A (τ_{S_1} = 1.7 ns) substituted with two –CO_2Me groups, the D-RC-A with –CO_2Me/–NMe_2 substitution exhibits a shorter (τ_{S_1} = 0.8 ns) lifetime of the S_1 state in toluene solution.[31] By resolving fs-TA data upon ultraviolet (UV) and visible excitation, the electronic relaxation channels of D-RC-A and A-RC-A are largely revealed. Moreover, by applying semi-classical Marcus theory, we determine that ISC of both D-RC-A and A-RC-A rely on a thermally activated $S_1 \rightarrow T_2$ transition rather than the channel that directly populates the T_1 state. We also report studies of singlet oxygen, $O_2(a^1\Delta_g)$, sensitization by A-RC-A, which provides additional insight into the excited-state behavior of this complex.

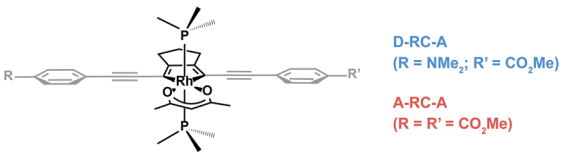

Scheme 1 Chemical structures of investigated D-RC-A and A-RC-A. The Rh(III)–ligand core is illustrated in black while the peripheral groups are in gray. The phosphine ligand is PMe_3.

Results and discussion

Static absorption spectra

The static absorption spectra of D-RC-A and A-RC-A in THF are displayed in Fig. 1 along with the calculated vertical excitation

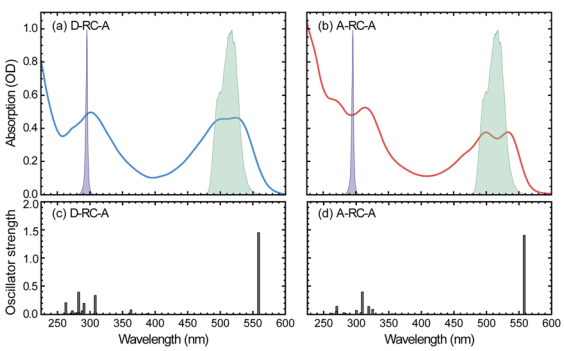

Fig. 1 (a and b) Static UV/visible absorption spectra of D-RC-A ((a), blue) and A-RC-A ((b), red) in THF solution (10^{-5} mol L^{-1}), overlapped with spectra of UV (violet shaded) and visible (green shaded) excitation pulses employed in the fs-TA experiments. (c and d) TD-DFT-calculated vertical excitation energies and oscillator strengths of D-RC-A (c) and A-RC-A (d).

energies and oscillator strengths, while the corresponding calculation results are listed in Table S2.† Note that the oscillator strength (f) here is not referenced to the transition probability for a freely oscillating electron in a single atom, but reflects only the transition dipole moment and the energy gap between two states of the RCPDs. For both D-RC-A and A-RC-A, the pronounced absorption in the 450–550 nm region can be attributed to the S_1 excited state, while higher singlet (S_m, $m > 1$) states comprise the intense absorption in the UV region. As a result, upon visible (λ_{ex} = 513 nm) and UV (λ_{ex} = 295 nm) optical excitation, direct population of the S_1 and S_m states can be expected in fs-TA experiments, as described in detail below.

The observed S_1 band of D-RC-A exhibits less pronounced vibronic progression than that of A-RC-A. Reduced vibronic progression might be attributed to stronger solute–solvent interaction due to excited-state charge transfer (CT) between substituted D and A groups, which was confirmed by natural transition orbital (NTO) analysis of the S_1 state of both RCPDs. As illustrated in Fig. S1,† A-RC-A exhibits a symmetric distribution of both hole and electron density in the S_1 state, indicating its locally excited (LE) nature. However, clear CT character is observed in the S_1 state NTOs of D-RC-A, *i.e.*, hole and electron density are asymmetrically distributed on D and A sides, respectively. A different S_1 character (CT or LE) of D-RC-A and A-RC-A can also affect the corresponding S_1 relaxation. The initially populated S_1 state undergoes rapid decay leading to the relaxed CT state, which is observed in the fs-TA signal of D-RC-A and absent for A-RC-A. Furthermore, NTO analysis on the triplet states indicates that the T_1 of D-RC-A is slightly mixed with CT character like the S_1 state, while the corresponding T_2 state and T_1/T_2 states of A-RC-A are all LE dominated.

On the other hand, NTO analysis indicates that the central Rh(III) in D-RC-A and A-RC-A is barely involved in the $S_0 \rightarrow S_1$, $S_0 \rightarrow T_1$, and $S_0 \rightarrow T_2$ transitions, which is consistent with previous reports on electronic transitions of RCPDs,[28,31] *i.e.*, the low-lying S_1, T_1, and T_2 states of RCPDs are dominated by π–π^* transitions of ligands with minimal contributions of Rh(III). The photophysics indicates the weak SOC of RCPDs, which is consistent with previous reports.[25–28,30,31] Without pronounced metal–ligand interaction, ISC dynamics of RCPDs are largely determined by energetic parameters (Γ and ΔE_{ST}) and can thus be discussed in the framework of semi-classical Marcus theory.

Excitation-wavelength-dependent fs-TA

To acquire a full picture of electronic relaxation of RCPDs, we performed fs-TA experiments on D-RC-A and A-RC-A upon excitation by either UV (λ_{ex} = 295 nm) or visible (λ_{ex} = 513 nm) laser pulses as previously reported.[50] The resulting TA signal in the probe range of λ_{pr} = 320–670 nm was recorded for delay times up to Δt = 3.8 ns and are displayed in Fig. 2.

As shown in Fig. 2a and b, D-RC-A exhibits nearly identical fs-TA signals upon UV (λ_{ex} = 295 nm) and visible (λ_{ex} = 513 nm) excitation, respectively, in which at least three distinct bands can be distinguished. The negative band appears immediately after excitation in the λ_{pr} = 470–550 nm regime and agrees with the static absorption spectrum ($S_0 \rightarrow S_1$), which can be

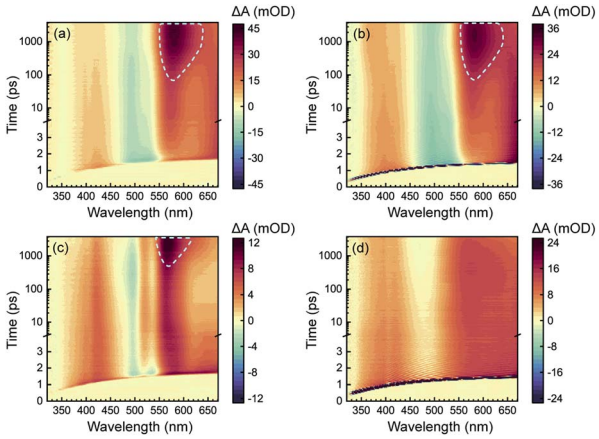

Fig. 2 Spectro-temporal maps of λ_{ex}-dependent fs-TA signals of D-RC-A upon UV (a) and visible (b) excitation as well as of A-RC-A upon identical UV (c) and visible (d) excitation. The spectral signatures of ISC-generated triplet states are highlighted by white dashed lines.

attributed to the ground-state bleaching (GSB) signal. At the same time, two excited-state absorption (ESA) bands of the S_1 state appear in the λ_{pr} = 360–460 nm and >550 nm regimes which, subsequently, exhibit relaxation simultaneously with the decay of the GSB band. Meanwhile, slow formation of a new positive band is observed with a center at λ_{pr} = 580 nm, which is superimposed on the decay of the long-lived ESA band in the λ_{pr} > 550 nm region, probably corresponding to ESA of an ISC-generated triplet state. However, the final destination (T_1 or T_2) of the observed ISC process is difficult to identify by fs-TA data itself. Instead, ISC rates of $S_1 \rightarrow T_1$ and $S_1 \rightarrow T_2$ need to be calculated to assign the observed ISC process. Thus, we tentatively denote the triplet state generated as the T_n ($n \geq 1$) state.

Unlike D-RC-A, A-RC-A exhibits λ_{ex}-dependent relaxation behavior. Upon UV excitation, a similar fs-TA signal as that for D-RC-A was recorded for A-RC-A, although the GSB displays a double peak at λ_{pr} = 500 nm and 535 nm, which is consistent with the pronounced vibronic progression exhibited in the static absorption spectrum. Meanwhile, triplet-state formation is also observed at λ_{pr} = 570 nm, with a substantially slower k_{ISC} than that of D-RC-A. As shown in Fig. S2,† preliminary fitting of triplet formation dynamics of D-RC-A (at λ_{pr} = 580 nm) and A-RC-A (at λ_{pr} = 570 nm) indicated that the observed ISC of D-RC-A (τ_{ISC} < 350 ps) is one order of magnitude faster than ISC of A-RC-A (τ_{ISC} > 3.5 ns). Thus, S_1 state relaxation of D-RC-A might be dominated by ISC as it is much faster than radiative and non-radiative $S_1 \rightarrow S_0$ channels. In contrast, considering the observed fluorescence lifetime (~1.7 ns), the radiative and non-radiative $S_1 \rightarrow S_0$ decay of A-RC-A might be comparable with ISC to triplet states.

Intriguingly, upon visible excitation, the triplet band of A-RC-A is absent in the fs-TA data up to the maximum delay time (3.8 ns), while the decay of ESA bands and refilling of the GSB band are still observable. In general, upon UV excitation, rapid internal conversion (IC) from initially populated S_m states leads to a vibrationally hot S_1 state. Compared with the S_1 state

directly populated by resonant visible excitation, excess vibrational energy of the S_1 state might be helpful to overcome the ISC barrier.[51–54] Therefore, we believe that the ISC barrier (E_a) for A-RC-A should be higher than that for D-RC-A, which is also indicated by a slower rise of the ISC band of A-RC-A compared to that of D-RC-A upon UV excitation.

Ultrafast electronic relaxation

To obtain details on the electronic relaxation of the RCPDs, we performed target analysis on the corresponding λ_{ex}-dependent fs-TA data. On ultrafast time scales, a sequential kinetic model including several independent species was employed for all fs-TA data, while a branched scheme was considered for the decay of the relaxed (CT and structural) S_1 state, corresponding to competition between relaxation to the S_0 state ($S_1 \rightarrow S_0$) and ISC to triplet states ($S_1 \rightarrow T_n$). As discussed above, S_1 relaxation of D-RC-A is dominated by the $S_1 \rightarrow T_n$ channel, for which the $S_1 \rightarrow S_0$ channel was correspondingly ignored in target analysis (Fig. S3†). However, for A-RC-A upon UV excitation, both the $S_1 \rightarrow S_0$ and $S_1 \rightarrow T_n$ channels were included in target analysis with a branch ratio of 0.5 (Fig. S3†). The extracted species-associated spectra (SAS) are displayed in Fig. 3, while the corresponding fitted time traces at selected λ_{pr} and the concentration evolution of each species can be found in Fig. S4 and S5,† respectively, in the ESI.†

As mentioned above, D-RC-A exhibits similar relaxation dynamics upon UV and visible excitation. Upon UV excitation, the populated S_m states undergo rapid IC with a time constant of $\tau_1 = 206$ fs to reach the Franck–Condon region of the S_1 state ($S_m \rightarrow S_1^{FC}$), which is absent in the fs-TA data upon resonant visible excitation to the S_1 state. The subsequent SAS exhibits a spectral depletion in the range $\lambda_{pr} = 570$–670 nm, which is consistent with fluorescence spectra of D-RC-A and can be attributed to the stimulated emission (SE) band of the S_1 state. Pronounced solvatochromism of D-RC-A has been reported,[31] implying CT character of the fluorescent bright state, which is also consistent with the NTO analysis mentioned above. Considering the observed SE signature in the SAS, we assigned the second SAS to the CT-relaxed S_1 state (noted as S_1^{CT}), corresponding to a local minimum on the S_1 potential energy surface (PES). Moreover, the fitted formation time of S_1^{CT} ($S_1^{FC} \rightarrow S_1^{CT}$, ~1 ps) is consistent with the reported formation time of the solvation-stabilized CT state of organic D–A-type chromophores in THF.[55,56]

During the subsequent relaxation ($S_1^{CT} \rightarrow S_1'$) with a ~10 ps time constant, the SAS exhibit only minimal changes of spectral features, which might be explained by structural relaxation in the S_1 state. In order to obtain further details on S_1 relaxation, we calculated the optimized structures of both D-RC-A and A-RC-A in their S_1, T_1, and T_2 states to be compared with the S_0 structure. As shown in Fig. S6 and S7,† large $S_0 \rightarrow S_1$ twisting is observed for the peripheral phenyl and D/A groups of RCPDs, which can be quantified by the calculated twisting angles listed in Table S3.† Apart from the twisting angles, contributions of $S_0 \rightarrow S_1$ conformational relaxation can be generalized in reorganization energy ($I^{S_1 \rightarrow S_0}$).[57,58] By summing over contributions from each vibrational mode (Fig. S8†), $I^{S_1 \rightarrow S_0}$ of D-RC-A and A-RC-A were calculated to be 1519 cm^{-1} and 1944 cm^{-1}, respectively. However, $I^{S_1 \rightarrow S_0}$ contributed by vibrational modes is not able to provide the relative contribution of each structural part of the RCPDs to conformational relaxation. Therefore, we further calculated the root-mean-square displacement (RMSD)

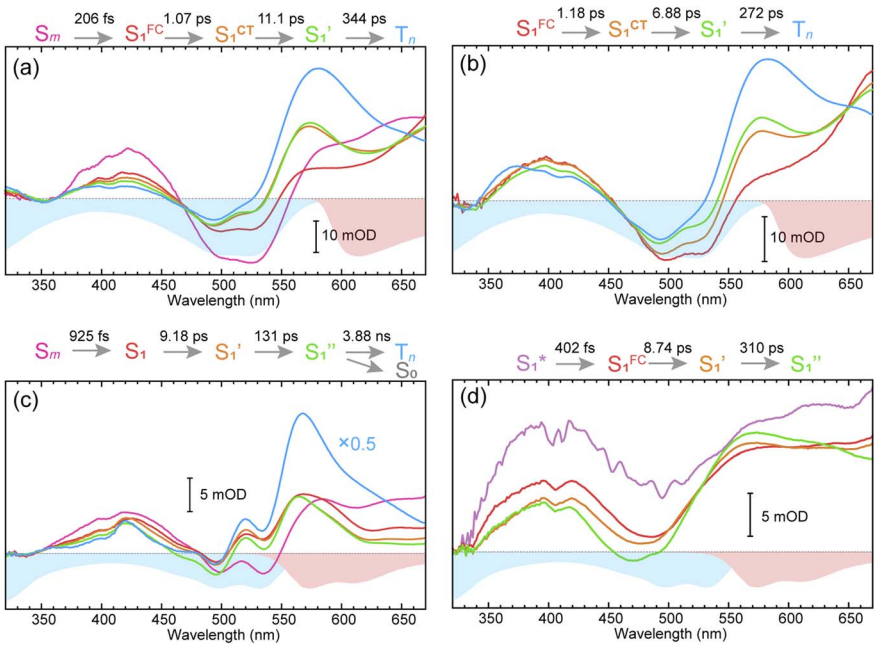

Fig. 3 Target-analysis-extracted species-associated spectra (SAS) of λ_{ex}-dependent fs-TA signals of D-RC-A upon 295 nm UV (a) and 513 nm visible (b) optical excitation, as well as SAS of A-RC-A upon identical UV (c) and visible (d) excitation. Four or five independent species were employed to reproduce the fs-TA signals.

in Cartesian coordinates of the optimized S_0 (x_i, y_i, z_i) and S_1 (x_i', y_i', z_i') state structures,

$$\mathrm{RMSD} = \sqrt{\frac{1}{N}\sum_{i}^{N}\left[\left(x_i - x_i'\right)^2 + \left(y_i - y_i'\right)^2 + \left(z_i - z_i'\right)^2\right]}, \quad (4)$$

Summing over all atoms, $i = 1, \ldots, N$. The calculation leads to $\mathrm{RMSD}^{S_1/S_0} = 0.156$ Å for D-RC-A which is lower than that for A-RC-A (0.207 Å), consistent with the calculated $I^{S_1 \to S_0}$. We further calculated the relative contributions of the peripheral groups (phenyls, C≡C, and D/A, gray part in Scheme 1) and Rh(III)–ligand core (black part in Scheme 1). For D-RC-A, the RMSD^{S_1/S_0} was found to be dominated by twisting of the peripheral parts of the structure with ~90% contribution. The rotational twisting around C–C single bonds has been widely reported to be nearly barrierless,[59,60] which is consistent with the observed efficient relaxation ($S_1^{CT} \to S_1'$, ~10 ps). Intriguingly, we found that the Rh(III)-ligand core contributes ~40% to the RMSD^{S_1/S_0} of A-RC-A *via* its own framework distortion, which is comparable with the twisting of the peripheral parts (~60%). Compared to the rapid twisting of the peripheral groups, the distortion of the molecular framework is normally much slower due to a high potential barrier. Therefore, a two-step conformational relaxation is expected to be observed in the fs-TA data of A-RC-A, which has been widely reported in organic fluorescent systems.[61–63]

The extracted species S_1' corresponds to a global minimum on the S_1-state PES, which subsequently undergoes ISC leading to formation of a triplet state, featured by the rise of intense absorption centered at $\lambda_{pr} = 580$ nm and the disappearance of SE depletion ($\lambda_{pr} = 570$–670 nm). The formation time ($S_1' \to T_n$, ~300 ps) of the triplet state corresponds to the ISC rate constant (k_{ISC}) of D-RC-A, which is consistent with the relatively low fluorescence quantum yield ($\Phi_f = 0.22$) and sub-nanosecond fluorescence lifetime ($\tau_{S_1} = 0.8$ ns) observed in toluene solution.[31] Note that relaxation of the S_1 state is contributed to by non-radiative decay to S_0 (k_{NR}^S), radiative decay to S_0 (k_R^S), and ISC to triplet states (k_{ISC}). Therefore, the S_1 ESA decay and GSB refilling dynamics could be largely different with formation of the triplet band, *i.e.*, S_1 ESA and GSB include contributions of k_{NR}^S, k_R^S, and k_{ISC}, while rising of the triplet band is associated with k_{ISC} only. The full picture of the electronic relaxation of the RCPDs is summarized in Fig. 4.

In the fs-TA data for A-RC-A upon UV excitation, we observed electronic relaxation that is significantly different from D-RC-A. Without a D–A structure, the CT state signature was absent in the fs-TA of A-RC-A. After excitation, rapid IC (~900 fs, $S_m \to S_1^{FC}$) is followed by two-step conformational relaxation ($S_1^{FC} \to S_1' \to S_1''$), corresponding to a comparable contribution of the peripheral structure and metal–ligand core to the RMSD^{S_1/S_0} of A-RC-A. The first step ($S_1^{FC} \to S_1'$, ~9 ps) exhibits a time constant similar to that of the corresponding step in D-RC-A ($S_1^{CT} \to S_1'$, ~10 ps), which was attributed to barrierless twisting of the peripheral structure. Note that the observed twisting with a ~10 ps time constant is unobservable in our previous time-resolved IR investigation due to the limitation of low temporal resolution (10–20 ps).[30] The subsequent step ($S_1' \to S_1''$, ~150 ps) accordingly corresponds to structural distortion of the Rh(III)–ligand framework. Furthermore, slower triplet formation ($S_1'' \to T_n$, ~3.88 ns) in A-RC-A than in D-RC-A was observed upon UV excitation, corresponding to a long-lived ($\tau_f = 1.7$ ns) S_1 state,[31] which is discussed in detail below. Upon ~25 fs visible excitation, A-RC-A exhibits largely different electronic relaxation (Fig. 3d) from the case with UV excitation (Fig. 3c). The target analysis extracted a short-lived species(noted as S_1^*) after excitation with a ~400 fs time constant. As described above, rapid IC (~900 fs, $S_m \to S_1^{FC}$) was identified for A-RC-A upon UV excitation, while the observed visible-excitation-induced ~400 fs relaxation obviously cannot be assigned to IC from S_m, as the visible excitation at $\lambda_{ex} = 513$ nm employed is resonant with the S_1 state of A-RC-A and, correspondingly, incapable of populating the S_m state. Moreover, as illustrated in Fig. S9,† we observed a beating behavior in the $\lambda_{pr} = 400$–550 nm wavelength regime of the fs-TA data, which is observed as an oscillatory modulation in both temporal (Fig. S4†) and frequency (Fig. S9†) domains. The beating-modulated TA spectra (Fig. S9†) observed in the initial few picoseconds are highly consistent with the extracted SAS of the S_1^* species with a ~400 fs relaxation. We therefore attribute S_1^* relaxation to dephasing of the coherent vibrational wave packet (noted as $S_1^* \to S_1^{FC}$). The dephasing of S_1^* was not recognized as an independent species

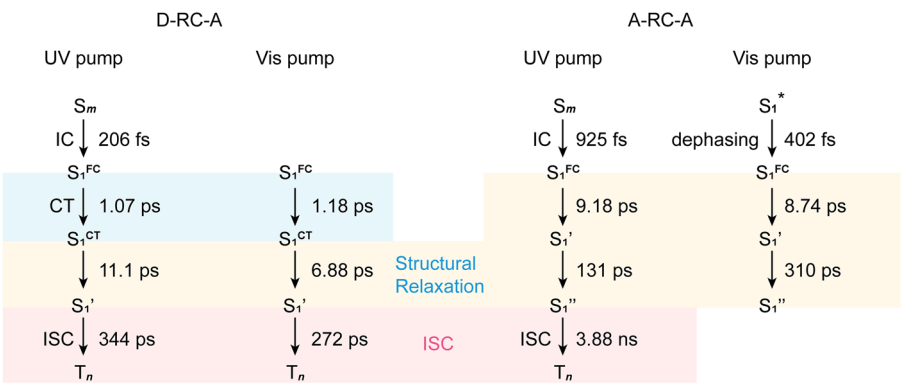

Fig. 4 Electronic relaxation of D-RC-A (left two panels) and A-RC-A (right two panels) revealed by λ_{ex}-dependent fs-TA measurements.

in the target analysis of D-RC-A upon visible excitation, which might be associated with a less modulated spectral shape and faster S_1^* dephasing (Fig. S9†) of D-RC-A due to intense solute–solvent interactions. We further extracted beating signals by subtracting the fitted exponential components from the measured fs-TA data. The Fourier transformed power spectra of the beating signals (Fig. S10†) revealed a dominant vibrational mode at ~250 cm^{-1} for both D-RC-A and A-RC-A. Considering that the beating frequency is independent of the 2,5-substitution, we speculate that the observed ~250 cm^{-1} mode might originate from a distortion of the metal–ligand core.

After rapid dephasing ($S_1^* \rightarrow S_1^{FC}$), the S_1 state of A-RC-A subsequently undergoes a two-step conformational relaxation ($S_1^{FC} \rightarrow S_1' \rightarrow S_1''$) nearly identical with that of A-RC-A upon UV excitation. However, the rise of the T_n band observed in the fs-TA of A-RC-A upon UV excitation is absent upon visible excitation. Instead, we observe an isosbestic point at $\lambda_{pr} = 530$ nm in the fs-TA data of A-RC-A upon visible excitation, indicating that the TA bands located on the blue (GSB, $\lambda_{pr} = 430$–530 nm) and red (ESA, $\lambda_{pr} = 530$–670 nm) sides of the isosbestic point belong to an identical process, *i.e.*, S_1 relaxation. However, note that the fs-TA observation cannot fully exclude the existence of ISC of A-RC-A upon visible excitation due to the limitation of the fs-TA time window. Actually, upon visible excitation, slight spectral rising can be observed between 550 nm and 600 nm at long delays, which is consistent with the triplet band observed upon UV excitation. A plausible explanation is that visible excitation leads to an ultraslow ISC which is unobservable within our time window (3.8 ns).

By measuring the fluorescence quantum yield of A-RC-A upon UV ($\Phi_f^{UV} = 0.29$) and visible ($\Phi_f^{vis} = 0.33$) excitation in THF (Table S4†) and assuming an unchanged radiative decay rate constant (k_r) upon different excitation, the ISC time constant upon visible excitation was estimated to be ~5.75 ns (ESI,† Section S4), which is accordingly unobservable in the fs-TA with time window of 3.8 ns. We also measured the fluorescence lifetime of A-RC-A upon UV ($\tau_{S_1}^{UV}$) and visible ($\tau_{S_1}^{vis}$) excitation, which leads to an unchanged lifetime of ~1.6 ns (Fig. S11–S13†). However, quantitative estimation of the S_1 state decay (ESI,† Section S4) indicated that $\tau_{S_1}^{vis}$ can be only <0.2 ns slower than $\tau_{S_1}^{UV}$, which can be easily concealed by different temporal profiles of excitation sources in the UV and visible regimes. Therefore, we believe an ultraslow ISC that is beyond our fs-TA time window leads to the absence of triplet ESA in the fs-TA of A-RC-A upon visible excitation, which corresponds to an inaccessible barrier for ISC. In the next section, we further analyze the ISC energetic diagram of D-RC-A and A-RC-A in the framework of Marcus theory to understand the fundamental mechanism that leads to the different ISC dynamics of D-RC-A and A-RC-A.

Marcus analysis of the ISC dynamics

As discussed above, upon identical excitation conditions, D-RC-A exhibited much faster ISC than A-RC-A, which is consistent with the reported lower Φ_f and shorter τ_{S_1} of D-RC-A compared to A-RC-A.[31] For systems with weak SOC, *i.e.*, $\langle S_m|\hat{H}_{SO}|T_n\rangle \ll E_a$, ISC can be simplified as a transition between non-adiabatic states and described by semi-classical Marcus theory.[64–66] As the basis for our Marcus analysis, adiabatic excitation energies of the S_1 and T_2 states were calculated with TD-DFT for both D-RC-A and A-RC-A, while the corresponding T_1 states were calculated using unrestricted DFT (UDFT). UDFT has been reported to be reliable for calculating T_1 states of organic and organometallic complexes, but is inherently not able to treat higher lying triplet states.[67–69]

Here, we first analyze the $S_1 \rightarrow T_1$ channel that is regarded as the dominant ISC channel in common organic systems,[70,71] for which the adiabatic excitation energies of the S_1 and T_1 states are required. The ISC barrier of the $S_1 \rightarrow T_1$ channel ($E_a^{S_1 \rightarrow T_1}$) was estimated by a reorganization energy ($I^{S_1 \rightarrow T_1}$) and corresponding adiabatic energy gap ($\Delta E_{ST}^{S_1 \rightarrow T_1}$) within the framework of Marcus theory. As listed in Table 1, $\Delta E_{ST}^{S_1 \rightarrow T_1}$ of RCPDs are comparable (0.829 eV for D-RC-A and 0.858 eV for A-RC-A) whereas D-RC-A features a higher $I^{S_1 \rightarrow T_1}$ (0.115 eV) than A-RC-A (0.062 eV), leading to $E_a^{S_1 \rightarrow T_1}$ for D-RC-A (1.103 eV) and A-RC-A (2.574 eV), which are comparable with the adiabatic energies of the corresponding T_1 states. Meanwhile, the SOC matrix elements $\langle S_1|\hat{H}_{SO}|T_1\rangle$ of D-RC-A and A-RC-A were calculated to be 4.045 cm^{-1} and 0.425 cm^{-1}, respectively. The large ISC barrier (>1 eV) leads to virtually forbidden transitions of the $S_1 \rightarrow T_1$ channel of D-RC-A and A-RC-A.

Table 1 Summary of the calculated and experimentally measured photophysical parameters associated with plausible ISC channels of D-RC-A and A-RC-A

	D-RC-A	A-RC-A
S_1 excitation energy[a]/eV	1.952	1.939
T_1 excitation energy[b]/eV	1.123	1.081
T_2 excitation energy[a]/eV	2.022	2.213
$RMSD^{S_1/S_0}$/Å	0.156	0.207
$RMSD^{S_1/T_1}$/Å	0.377	0.302
$RMSD^{S_1/T_2}$/Å	0.853	0.325
$I^{S_1 \rightarrow S_0}$/eV	0.188	0.241
$I^{S_1 \rightarrow T_1}$/eV	0.115	0.062
$I^{T_2 \rightarrow S_1}$/eV	0.558	0.257
[c]$\Delta E_{ST}^{S_1 \rightarrow T_1}$/eV	0.829	0.858
[c]$\Delta E_{ST}^{S_1 \rightarrow T_2}$/eV	−0.070	−0.274
[c]$\Delta E_{TS}^{T_2 \rightarrow S_1}$/eV	0.070	0.274
$\langle S_1|\hat{H}_{SO}|T_1\rangle$/$cm^{-1}$	4.045	0.425
$\langle S_1|\hat{H}_{SO}|T_2\rangle$/$cm^{-1}$	4.481	8.697
[d]$E_a^{S_1 \rightarrow T_1}$/eV	1.103	2.574
[d]$E_a^{T_2 \rightarrow S_1}$/eV	0.106	<0.001
[e]$E_a^{S_1 \rightarrow T_2}$/eV	0.177	0.274
$E_a^{S_1 \rightarrow T_1}/E_a^{S_1 \rightarrow T_2}$	6.325	9.387
$k_{ISC}^{S_1 \rightarrow T_2}$ (cal. DA)/$k_{ISC}^{S_1 \rightarrow T_2}$ (cal. AA)	7.774	
k_{ISC} (exp.)/ps^{-1}	1/350	1/3900
k_{ISC} (exp. DA)/k_{ISC} (exp. AA)	11.143	

[a] Adiabatic excitation energy calculated by TD-DFT. [b] Adiabatic excitation energy calculated by UDFT. [c] Calculated by adiabatic energies of optimized geometries of corresponding electronic states, the adiabatic energy gap of an exothermic process was defined to be positive. [d] Estimated by reorganization energy and adiabatic energy gap of the corresponding transition by Marcus theory. [e] Calculated by $E_a^{S_1 \rightarrow T_2} = E_a^{T_2 \rightarrow S_1} + \Delta E_{TS}^{T_2 \rightarrow S_1}$.

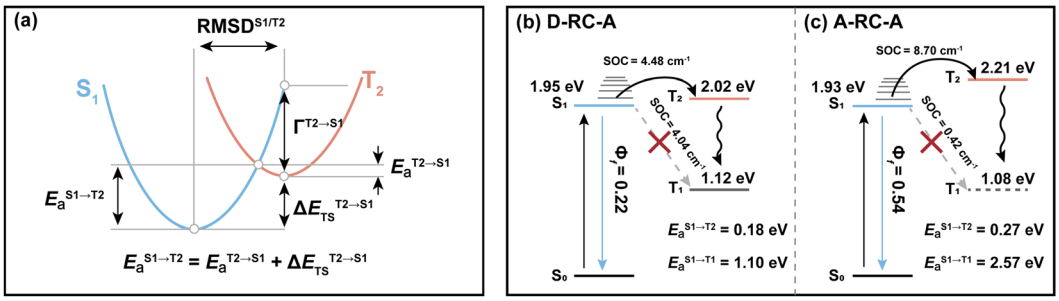

Fig. 5 (a) Simplified energetic diagram for calculating the ISC barrier of the $S_1 \rightarrow T_2$ transition in the framework of Marcus theory, and energy diagrams for plausible ISC channels of D-RC-A (b) and A-RC-A (c), in which both T_1 and T_2 states are considered.

Regarding the $S_1 \rightarrow T_2$ channel, the calculated adiabatic energies of the S_1 and T_2 states indicate its endothermic nature with a negative $\Delta E_{ST}^{S_1 \rightarrow T_2}$ for both D-RC-A (−0.070 eV) and A-RC-A (−0.274 eV). Nevertheless, the $S_1 \rightarrow T_2$ transition of RCPDs can still be accessible through a thermally activated mechanism as long as $E_a^{S_1 \rightarrow T_2}$ is small enough (normally <0.2 eV), which has been observed *via* temperature-dependent experiments for RCPDs.[28] To estimate $E_a^{S_1 \rightarrow T_2}$, as illustrated in Fig. 5a, we calculated the reorganization energy ($\lambda^{T_2 \rightarrow S_1}$) and adiabatic energy gap ($\Delta E_{TS}^{T_2 \rightarrow S_1}$) of its reverse transition $T_2 \rightarrow S_1$. As an exothermic process, $E_a^{T_2 \rightarrow S_1}$ can be estimated by Marcus theory, leading to $E_a^{T_2 \rightarrow S_1}$ = 0.106 eV and <0.001 eV for D-RC-A and A-RC-A, respectively. Thus, $E_a^{S_1 \rightarrow T_2}$ can be approximated by the sum of $E_a^{T_2 \rightarrow S_1}$ and the adiabatic energy gap ($\Delta E_{TS}^{T_2 \rightarrow S_1}$), *i.e.*, 0.177 eV and 0.274 eV for D-RC-A (Fig. 5b) and A-RC-A (Fig. 5c), respectively.

With the calculated ISC barriers and SOC matrix elements of plausible ISC channels, we can discuss the ISC dynamics of D-RC-A (Fig. 5b) and A-RC-A (Fig. 5c) in detail. For both D-RC-A and A-RC-A, $E_a^{S_1 \rightarrow T_1}$ is substantially higher than $E_a^{S_1 \rightarrow T_2}$ ($E_a^{S_1 \rightarrow T_1}/E_a^{S_1 \rightarrow T_2}$ = 6.325 for D-RC-A and 9.387 for A-RC-A), leading to $S_1 \rightarrow T_2$ as the dominant ISC channel of both D-RC-A and A-RC-A. Although $S_1 \rightarrow T_2$ ISC is an endothermic process, the thermally accessible barriers (~0.2 eV) lead to ISC dynamics at room temperature, which is consistent with our previously observed temperature-dependence.[28] Furthermore, $k_{ISC}^{S_1 \rightarrow T_2}$ of D-RC-A were calculated to be ~7.7 times faster than $k_{ISC}^{S_1 \rightarrow T_2}$ of A-RC-A, which is perfectly consistent with the ~11 times faster ISC observed experimentally by fs-TA. The relatively fast ISC of D-RC-A also explains the lower Φ_f of D-RC-A than A-RC-A due to competition between radiative and non-radiative (including ISC) decay of the S_1 state. Meanwhile, the calculated ISC barrier ($E_a^{S_1 \rightarrow T_2}$) of D-RC-A and A-RC-A also explains the λ_{ex}-dependent fs-TA data of A-RC-A. For D-RC-A, the thermally accessible $S_1 \rightarrow T_2$ channel at room temperature ($E_a^{S_1 \rightarrow T_2}$ = 0.177 eV) leads to the observed λ_{ex}-independent ISC signature in the TA-data. However, $E_a^{S_1 \rightarrow T_2}$ of A-RC-A (0.274 eV) is ~0.1 eV higher than that for the ISC channel of D-RC-A, leading to a hindered ISC ($S_1 \rightarrow T_2$) *via* a thermally activated mechanism. As discussed above, triplet ESA was consequently unobservable in the fs-TA of A-RC-A upon visible excitation due to its slow formation (~5.8 ns). However, upon UV excitation, initial IC ($S_m \rightarrow S_1$) decay may lead to more population being distributed in higher vibrational levels of the S_1 state, leading to faster ISC that can be observed in the fs-TA data. Note that values of all ISC barriers listed in Table 1 were estimated by Marcus theory based on the TD-DFT-calculated energies of S_1 and T_2 states, and unrestricted DFT (UDFT)-calculated T_1 state, which can have errors up to 0.3 eV. Thus, the $S_1 \rightarrow T_2$ ISC barrier ($E_a^{S_1 \rightarrow T_2}$) can possibly be different between D-RC-A and A-RC-A, leading to different observations in the λ_{ex}-dependent fs-TA data.

Last but not least, note that although the T_2 state is heavily involved in the ISC dynamics of D-RC-A and A-RC-A, we believe that the observed triplet signal at λ_{pr} = 570–580 nm in the fs-TA data must be assigned to the T_1 rather than the T_2 state. Spin-allowed $T_2 \rightarrow T_1$ transitions with ~1 eV energy gaps are expected to be much faster than the corresponding $S_1 \rightarrow T_2$ transitions, leading to limited accumulation of T_2 species. Thus, the observed ESA bands should be assigned to the T_1 states formed through rapid decay from the T_2 state. Similarly, the ISC populated T_2 states are energetically higher than the corresponding S_1 states of D-RC-A and A-RC-A, leading to potential exothermic reverse ISC (RISC, $T_2 \rightarrow S_1$). However, such an RISC process cannot be the dominant decay channel of the T_2 state due to competition of spin-allowed internal conversion ($T_2 \rightarrow T_1$).

Singlet oxygen sensitization

Having the above fs-TA and theoretical data in hand, we then examined the ability of photoexcited A-RC-A to sensitize singlet molecular oxygen, $O_2(a^1\Delta_g)$, and the associated kinetics for two reasons: (1) this would likely provide additional information on the formation of triplet states upon light irradiation, and (2) a compound which is both fluorescent and can generate $O_2(a^1\Delta_g)$ from its triplet state could be potentially useful for

Table 2 $O_2(a^1\Delta_g)$ quantum yields, Φ_Δ, for A-RC-A[a]

Gas	Φ_Δ
2% O_2	0.10
21% O_2	0.18
40% O_2	0.23
70% O_2	0.32
100% O_2	0.34

[a] Errors on Φ_Δ are ± 10%. Data for the pertinent experiments are shown in Fig. 6.

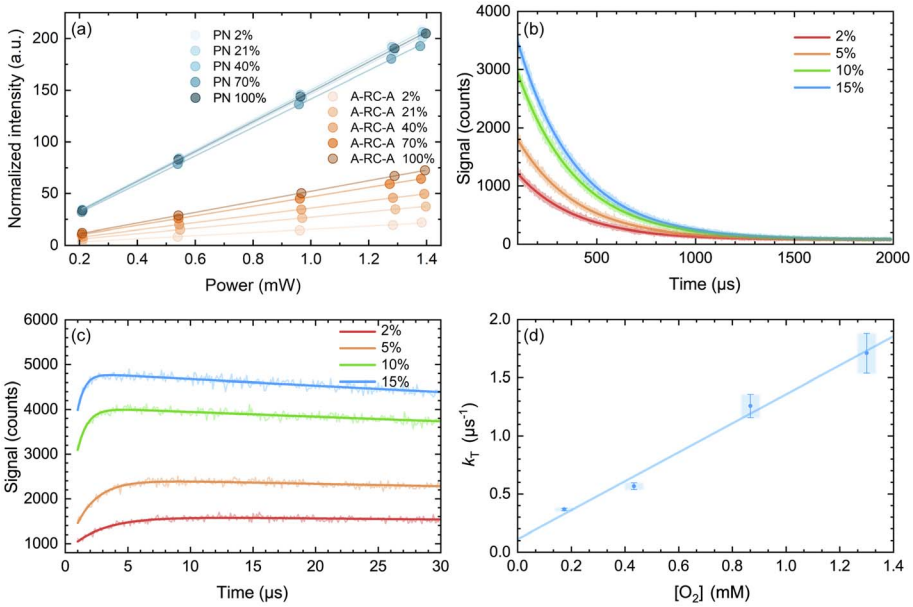

Fig. 6 (a) Integrated intensity of the $O_2(a^1\Delta_g)$ phosphorescence signal upon irradiation at 417 nm, normalized by the sensitizer absorbance and the $O_2(a^1\Delta_g)$ lifetime, plotted as a function of laser power and collected over a range of O_2 concentrations for both A-RC-A and for the reference standard, phenalenone (PN), in toluene-d_8. The O_2 concentration is represented as the percent of O_2 in the O_2/N_2 gas mixture bubbled through the solution. The slopes of the linear fits are proportional to the $O_2(a^1\Delta_g)$ quantum yield. Representative time-resolved $O_2(a^1\Delta_g)$ phosphorescence traces used to obtain the A-RC-A data are shown in (b and c). (b) The data from 100 μs to 2000 μs were fitted by a single exponential decay function (solid lines) to obtain the lifetime of $O_2(a^1\Delta_g)$ (*i.e.*, $1/k_\Delta$). (c) Using k_Δ as a fixed parameter, eqn (5) was used as a fitting function (solid lines) to obtain values of k_T for a time domain where $O_2(a^1\Delta_g)$ was formed in the photosensitized reaction. (d) Plot of k_T, obtained from the fits shown in (c) for the A-RC-A data, against the concentration of dissolved oxygen. The slope, $(1.3 \pm 0.1) \times 10^9$ M^{-1} s^{-1}, is the bimolecular rate constant for oxygen quenching of the $O_2(a^1\Delta_g)$ precursor. The intercept yields a value of ~9 μs for the lifetime of this $O_2(a^1\Delta_g)$ precursor in the absence of oxygen. Both of these numbers are consistent with expectation for oxygen quenching of a triplet state.[74,82]

both bio-imaging and photodynamic therapy.[72,73] Moreover, using the fluorescence, one has the advantage of being able to insure that the sensitizing compound was localized at the desired location in a heterogeneous biological system.[74] We note that in our previous studies,[28,30] we found that several related complexes are capable of simultaneous fluorescence and $O_2(a^1\Delta_g)$ sensitization, with reasonable quantum yields for both processes, often summing to *ca.* 1.

Quantum yields of $O_2(a^1\Delta_g)$ production, Φ_Δ, were obtained by monitoring the intensity of the 1275 nm $O_2(a^1\Delta_g) \rightarrow O_2(X^3\Sigma_g^-)$ phosphorescence in time-resolved experiments, as described previously.[75,76] Experiments were performed upon irradiation of A-RC-A at 417 nm. The integrated intensity of the time-resolved $O_2(a^1\Delta_g)$ phosphorescence signal, measured as a function of incident laser power, was normalized by the sensitizer absorbance and the $O_2(a^1\Delta_g)$ lifetime. Although a bleaching experiment indicates that A-RC-A can react with $O_2(a^1\Delta_g)$ (Fig. S14†), all data were recorded under conditions where A-RC-A bleaching was negligible.

We first performed experiments in toluene-h_8, using a solution that had been bubbled with a gas stream containing 2% oxygen and 98% N_2 (the reasons for using low concentrations of oxygen will become apparent below when discussing the kinetics of the time-resolved $O_2(a^1\Delta_g)$ phosphorescence signal). In this case, we performed one set of experiments using 1*H*-phenalenone (PN) in benzene as the reference $O_2(a^1\Delta_g)$ photosensitizer ($\Phi_\Delta = 0.92 \pm 0.03$),[77,78] and another using *m*-tetraphenylporphyrin (TPP) in benzene as the reference photosensitizer ($\Phi_\Delta = 0.66 \pm 0.08$).[79] The results yield a value of Φ_Δ for A-RC-A of 0.09 ± 0.01. The pertinent data are shown in Fig. S15 and S16.†

Singlet oxygen phosphorescence data recorded upon irradiation of A-RC-A show an increase in the value of Φ_Δ with increasing oxygen concentration (Table 2). In contrast, corresponding data from the PN-sensitized production of $O_2(a^1\Delta_g)$ do not show an increase in Φ_Δ with an increase in the oxygen concentration (Fig. 6a). These data indicate that, in the PN experiment, the lifetime of the $O_2(a^1\Delta_g)$ precursor (*i.e.*, the PN triplet state) is sufficiently long that the entire ^{3}PN population is effectively quenched at a low oxygen concentration, which is consistent with expectation. For the A-RC-A experiment, the data indicate that the $O_2(a^1\Delta_g)$ precursor, presumably the A-RC-A triplet state, is sufficiently short-lived that higher oxygen concentrations are needed to quench a larger fraction of the ^{3}A-RC-A population.

Given that the lifetime of the S_1 state of A-RC-A in oxygen-free toluene is 1.7 ns, the S_1 state is so short-lived that it cannot be quenched by oxygen, even in an oxygen-saturated solution at atmospheric pressure. This can be confirmed in a calculation where one accepts that the quenching will occur at the diffusion controlled limit (*i.e.*, $k_{diff} = 3 \times 10^{10}$ M^{-1} s^{-1}). As such, we infer that the $O_2(a^1\Delta_g)$ precursor will be the A-RC-A triplet state (*vide*

infra). We then chose to obtain information about the kinetics of the $O_2(a^1\Delta_g)$ precursor, again presumably the A-RC-A triplet state, using our time-resolved $O_2(a^1\Delta_g)$ phosphorescence data, as described below.

For the triplet-state-photosensitized production of $O_2(a^1\Delta_g)$ in homogeneous solutions, the intensity, $I(t)$, of the time-resolved 1275 nm $O_2(a^1\Delta_g) \rightarrow O_2(X^3\Sigma_g^-)$ phosphorescence signal is generally modeled using a fitting function based on eqn (5)[74,75,81]

$$I(t) = \frac{I_{tot}}{k_\Delta - k_T}\left[e^{-k_T t} - e^{-k_\Delta t}\right]. \quad (5)$$

In eqn (5), I_{tot} is proportional to the total integrated intensity of $O_2(a^1\Delta_g)$ phosphorescence, k_T is the decay rate constant for the $O_2(a^1\Delta_g)$ precursor (*i.e.*, the reciprocal lifetime of the sensitizer triplet state) and k_Δ the rate constant for $O_2(a^1\Delta_g)$ decay (*i.e.*, the reciprocal $O_2(a^1\Delta_g)$ lifetime). By performing the $O_2(a^1\Delta_g)$ phosphorescence experiment in toluene-d_8 as opposed to toluene-h_8, we take advantage of the large H/D solvent isotope effect on the $O_2(a^1\Delta_g)$ lifetime.[74] In this way, we can independently characterize k_Δ in a time domain where k_T does not appreciably influence the signal (Fig. 6b). Using this value of k_Δ as a fixed parameter, we can then re-fit the $O_2(a^1\Delta_g)$ phosphorescence data in the time domains where k_T influences the signal (Fig. 6c). We applied this procedure for experiments performed using a series of comparatively low oxygen concentrations to assess more accurately the decay rate constant of the $O_2(a^1\Delta_g)$ precursor.

In Fig. 6d, we plot the values of k_T thus obtained for A-RC-A against the oxygen concentration to yield the bimolecular rate constant for oxygen quenching of the $O_2(a^1\Delta_g)$ precursor. We determined oxygen concentrations using the mole fraction of oxygen in the bubbling gas (controlled by O_2 and N_2 flow meters) and Henry's Law constants published by Battino, *et al.*[82] The value obtained for this quenching rate constant is $(1.3 \pm 0.1) \times 10^9$ M^{-1} s^{-1}. As an independent control for this study on A-RC-A, we performed the same experiment using PN as the $O_2(a^1\Delta_g)$ sensitizer (Fig. S17†), and the results obtained provide credence for our results on A-RC-A. Specifically, our data for the quenching of ^{3}PN by oxygen yield a rate constant of $(2.2 \pm 0.2) \times 10^9$ M^{-1} s^{-1}, which is consistent with published data.[78]

The data obtained from Fig. 6d are consistent with the following assignment: the $O_2(a^1\Delta_g)$ precursor upon irradiation of A-RC-A is a triplet state whose lifetime in the absence of oxygen is ~9 μs.

From Fig. 6b, the values of the $O_2(a^1\Delta_g)$ lifetime obtained (*i.e.*, $k_\Delta^{-1} = 296 \pm 3$ μs) are shorter than what is expected for the solvent-mediated deactivation of $O_2(a^1\Delta_g)$ in toluene-d_8. For the latter, we independently recorded a value of 326 ± 3 μs using PN as the sensitizer with the same batch of toluene-d_8 used for the A-RC-A experiments. Using eqn (6), and with the A-RC-A concentration of 1.7×10^{-5} M used in our experiments, we obtain a rate constant of $\sim 1.8 \times 10^7$ M^{-1} s^{-1} for the deactivation/removal of $O_2(a^1\Delta_g)$ by A-RC-A. Given the magnitude of this rate constant, it is likely that the mechanism for A-RC-A-mediated deactivation of $O_2(a^1\Delta_g)$ involves some charge transfer from A-RC-A to $O_2(a^1\Delta_g)$.[74,80] Moreover, based on an A-RC-A bleaching experiment (Fig. S14†), a small component of this rate constant reflects a chemical reaction between A-RC-A and $O_2(a^1\Delta_g)$.

$$k_\Delta^{\text{obs.with A-RC-A}} = k_\Delta^{\text{obs.without A-RC-A}} + k_q[\text{A-RC-A}] \quad (6)$$

We also considered the interesting possibility that the $O_2(a^1\Delta_g)$ precursor might possibly be the T_2 state. However, our data indicate that the $O_2(a^1\Delta_g)$ precursor upon irradiation of A-RC-A has quite a long lifetime (~9 μs obtained from the intercept of the plot in Fig. 6d) and, as such, it must be the T_1 state, as spin-allowed internal conversion from T_2 to T_1 is expected to be quite rapid (*vide supra*).

Conclusions

We investigated the ultrafast photophysics and intersystem crossing (ISC) dynamics of two *para*-substituted 2,5-bis(phenylethynyl) RCPDs (D-RC-A and A-RC-A) using excitation-wavelength-dependent fs-TA measurements and TD-DFT calculations. The electronic relaxation channels of the S_1 state were revealed in detail, including charge transfer, conformational relaxation, vibrational dephasing, and ISC. By calculating the thermodynamic barrier and spin–orbit coupling, plausible ISC channels were revealed using semi-classical Marcus theory, *i.e.*, ISC is dominated by the thermally activated $S_1 \rightarrow T_2$ channel. With weak metal–ligand interactions, the plausible ISC channels of RCPDs are largely affected by ISC barriers. Studies of the sensitization of $O_2(a^1\Delta_g)$ by A-RC-A give quantum yields Φ_Δ of up to ~0.3 at high oxygen concentrations, consistent with the rate of ISC being competitive with that of fluorescence. The relatively long lifetime of the triplet state responsible for sensitization of $O_2(a^1\Delta_g)$ of ~9 μs indicates that it must be T_1, being formed rapidly from T_2. Our work, especially the paradigm on ISC dynamics, might provide useful insight into the behavior of other fluorescent emitters.

Data availability

The data supporting this article have been included as part of the ESI.†

Author contributions

Zilong Guo: conceptualization, methodology, investigation, data curation, formal analysis, visualization and writing original draft; Yaxin Wang: data curation, formal analysis and validation; Julia Heitmüller: data curation and formal analysis; Carolin Sieck: investigation and data curation; Andreas Prüfer: investigation and data curation; Philipp Ralle: investigation and data curation; Andreas Steffen: conceptualization, methodology, investigation, writing – review and editing; Petr Henke: methodology, data curation, formal analysis and validation; Peter R. Ogilby: methodology, supervision, and writing – review and editing; Todd B. Marder: conceptualization, formal analysis, funding acquisition, supervision, and writing – review and editing; Xiaonan Ma: conceptualization, formal analysis,

funding acquisition, supervision, and writing – review and editing; Tobias Brixner: conceptualization, formal analysis, funding acquisition, supervision, and writing – review and editing.

Conflicts of interest

There are no conflicts to declare.

Acknowledgements

X. M. thanks the National Key R&D Program of China (No. 2020YFA0714603 and 2020YFA0714604) for funding. T. B. M. thanks the Julius-Maximilians-Universität Würzburg for support.

Notes and references

1 D. M. Arias-Rotondo and J. K. McCusker, *Chem. Soc. Rev.*, 2016, **45**, 5803–5820.
2 D. A. Nicewicz and D. W. C. MacMillan, *Science*, 2008, **322**, 77–80.
3 F. Strieth-Kalthoff, M. J. James, M. Teders, L. Pitzer and F. Glorius, *Chem. Soc. Rev.*, 2018, **47**, 7190–7202.
4 Y. Du, R. M. Pearson, C.-H. Lim, S. M. Sartor, M. D. Ryan, H. Yang, N. H. Damrauer and G. M. Miyake, *Chem.–Eur. J.*, 2017, **23**, 10962–10968.
5 X. Zhao, Y. Hou, L. Liu and J. Zhao, *Energy Fuels*, 2021, **35**, 18942–18956.
6 K. Y. Zhang, H.-W. Liu, M.-C. Tang, A. W.-T. Choi, N. Zhu, X.-G. Wei, K.-C. Lau and K. K.-W. Lo, *Inorg. Chem.*, 2015, **54**, 6582–6593.
7 A. Kazama, Y. Imai, Y. Okayasu, Y. Yamada, J. Yuasa and S. Aoki, *Inorg. Chem.*, 2020, **59**, 6905–6922.
8 D. Siegmund, N. Lorenz, Y. Gothe, C. Spies, B. Geissler, P. Prochnow, P. Nuernberger, J. E. Bandow and N. Metzler-Nolte, *Dalton Trans.*, 2017, **46**, 15269–15279.
9 K. Y. Zhang, P. Gao, G. Sun, T. Zhang, X. Li, S. Liu, Q. Zhao, K. K.-W. Lo and W. Huang, *J. Am. Chem. Soc.*, 2018, **140**, 7827–7834.
10 X. Zhang, Y. Hou, X. Xiao, X. Chen, M. Hu, X. Geng, Z. Wang and J. Zhao, *Coord. Chem. Rev.*, 2020, **417**, 213371.
11 D. Di, A. S. Romanov, L. Yang, J. M. Richter, J. P. H. Rivett, S. Jones, T. H. Thomas, M. Abdi Jalebi, R. H. Friend, M. Linnolahti, M. Bochmann and D. Credgington, *Science*, 2017, **356**, 159–163.
12 S.-F. Wang, B.-K. Su, X.-Q. Wang, Y.-C. Wei, K.-H. Kuo, C.-H. Wang, S.-H. Liu, L.-S. Liao, W.-Y. Hung, L.-W. Fu, W.-T. Chuang, M. Qin, X. Lu, C. You, Y. Chi and P.-T. Chou, *Nat. Photonics*, 2022, **16**, 843–850.
13 Y.-C. Wei, S. F. Wang, Y. Hu, L.-S. Liao, D.-G. Chen, K.-H. Chang, C.-W. Wang, S.-H. Liu, W.-H. Chan, J.-L. Liao, W.-Y. Hung, T.-H. Wang, P.-T. Chen, H.-F. Hsu, Y. Chi and P.-T. Chou, *Nat. Photonics*, 2020, **14**, 570–577.
14 S.-F. Wang, D.-Y. Zhou, K.-H. Kuo, C.-H. Wang, C.-M. Hung, J. Yan, L.-S. Liao, W.-Y. Hung, Y. Chi and P.-T. Chou, *Angew. Chem., Int. Ed.*, 2024, **63**, e202317571.
15 M. Chergui, *Acc. Chem. Res.*, 2015, **48**, 801–808.
16 W. Gawelda, A. Cannizzo, V.-T. Pham, F. van Mourik, C. Bressler and M. Chergui, *J. Am. Chem. Soc.*, 2007, **129**, 8199–8206.
17 A. Cannizzo, F. van Mourik, W. Gawelda, G. Zgrablic, C. Bressler and M. Chergui, *Angew. Chem., Int. Ed.*, 2006, **45**, 3174–3176.
18 Ch. Bressler, C. Milne, V.-T. Pham, A. ElNahhas, R. M. van der Veen, W. Gawelda, S. Johnson, P. Beaud, D. Grolimund, M. Kaiser, C. N. Borca, G. Ingold, R. Abela and M. Chergui, *Science*, 2009, **323**, 489–492.
19 Q. Sun, S. Mosquera-Vazquez, L. M. Lawson Daku, L. Guénée, H. A. Goodwin, E. Vauthey and A. Hauser, *J. Am. Chem. Soc.*, 2013, **135**, 13660–13663.
20 A. J. Atkins and L. González, *J. Phys. Chem. Lett.*, 2017, **8**, 3840–3845.
21 Y. Sun, S. Doria, X. Xiao, L. Bussotti, Y. Li, J. Zhao and M. D. Donato, *J. Organomet. Chem.*, 2024, **1006**, 123004.
22 J. Moll, R. Naumann, L. Sorge, C. Förster, N. Gessner, L. Burkhardt, N. Ugur, P. Nuernberger, W. Seidel, C. Ramanan, M. Bauer and K. Heinze, *Chem.–Eur. J.*, 2022, **28**, e202201858.
23 R. D. Dill, R. I. Portillo, S. G. Shepard, M. P. Shores, A. K. Rappé and N. H. Damrauer, *Inorg. Chem.*, 2020, **59**, 14706–14715.
24 S. M. Fatur, S. G. Shepard, R. F. Higgins, M. P. Shores and N. H. Damrauer, *J. Am. Chem. Soc.*, 2017, **139**, 4493–4505.
25 C. Sieck, D. Sieh, M. Sapotta, M. Haehnel, K. Edkins, A. Lorbach, A. Steffen and T. B. Marder, *J. Organomet. Chem.*, 2017, **847**, 184–192.
26 J. P. Rourke, A. S. Batsanov, J. A. K. Howard and T. B. Marder, *Chem. Commun.*, 2001, 2626–2627.
27 A. Steffen, R. M. Ward, M. G. Tay, R. M. Edkins, F. Seeler, M. van Leeuwen, L.-O. Pålsson, A. Beeby, A. S. Batsanov, J. A. K. Howard and T. B. Marder, *Chem.–Eur. J.*, 2014, **20**, 3652–3666.
28 A. Steffen, K. Costuas, A. Boucekkine, M.-H. Thibault, A. Beeby, A. S. Batsanov, A. Charaf-Eddin, D. Jacquemin, J.-F. Halet and T. B. Marder, *Inorg. Chem.*, 2014, **53**, 7055–7069.
29 K. Li, Y. Chen, J. Wang and C. Yang, *Coord. Chem. Rev.*, 2021, **433**, 213755.
30 A. Steffen, M. G. Tay, A. S. Batsanov, J. A. K. Howard, A. Beeby, K. Q. Vuong, X.-Z. Sun, M. W. George and T. B. Marder, *Angew. Chem., Int. Ed.*, 2010, **122**, 2399–2403.
31 C. Sieck, M. G. Tay, M.-H. Thibault, R. M. Edkins, K. Costuas, J.-F. Halet, A. S. Batsanov, M. Haehnel, K. Edkins, A. Lorbach, A. Steffen and T. B. Marder, *Chem.–Eur. J.*, 2016, **22**, 10523–10532.
32 T. Kumpulainen, B. Lang, A. Rosspeintner and E. Vauthey, *Chem. Rev.*, 2017, **117**, 10826–10939.
33 O. P. Dimitriev, *Chem. Rev.*, 2022, **122**, 8487–8593.
34 V. Lawetz, G. Orlandi and W. Siebrand, *J. Chem. Phys.*, 1972, **56**, 4058–4072.
35 G. W. Robinson and R. P. Frosch, *J. Chem. Phys.*, 1963, **38**, 1187–1203.

36 P. K. Samanta, D. Kim, V. Coropceanu and J.-L. Brédas, *J. Am. Chem. Soc.*, 2017, **139**, 4042–4051.
37 J.-L. Brédas, D. Beljonne, V. Coropceanu and J. Cornil, *Chem. Rev.*, 2004, **104**, 4971–5004.
38 K. Schmidt, S. Brovelli, V. Coropceanu, D. Beljonne, J. Cornil, C. Bazzini, T. Caronna, R. Tubino, F. Meinardi, Z. Shuai and J.-L. Brédas, *J. Phys. Chem. A*, 2007, **111**, 10490–10499.
39 M. Bixon and J. Jortner, in *Advances in Chemical Physics*, John Wiley & Sons, Ltd, 1999, pp. 35–202.
40 R. A. Marcus and N. Sutin, *Biochim. Biophys. Acta, Bioenerg.*, 1985, **811**, 265–322.
41 R. A. Marcus, *Rev. Mod. Phys.*, 1993, **65**, 599–610.
42 Y. Liu, M. Lin and Y. Zhao, *J. Phys. Chem. A*, 2017, **121**, 1145–1152.
43 J. Stubbe, D. G. Nocera, C. S. Yee and M. C. Y. Chang, *Chem. Rev.*, 2003, **103**, 2167–2202.
44 E. Y.-T. Li, T.-Y. Jiang, Y. Chi and P.-T. Chou, *Phys. Chem. Chem. Phys.*, 2014, **16**, 26184–26192.
45 T. J. Penfold, E. Gindensperger, C. Daniel and C. M. Marian, *Chem. Rev.*, 2018, **118**, 6975–7025.
46 V. Pomogaev, S. Chiodo, K. Ruud, R. Kuznetsova and P. Avramov, *J. Phys. Chem. C*, 2020, **124**, 11100–11109.
47 N. Aizawa, Y. Harabuchi, S. Maeda and Y.-J. Pu, *Nat. Commun.*, 2020, **11**, 3909.
48 K. Li, G. S. M. Tong, J. Yuan, C. Ma, L. Du, C. Yang, W.-M. Kwok, D. L. Phillips and C.-M. Che, *Inorg. Chem.*, 2020, **59**, 14654–14665.
49 Q. Zhu, S. Feng, X. Guo, X. Chen and J. Zhang, *Spectrochim. Acta, Part A*, 2019, **221**, 117214.
50 X. Ma, J. Maier, M. Wenzel, A. Friedrich, A. Steffen, T. B. Marder, R. Mitrić and T. Brixner, *Chem. Sci.*, 2020, **11**, 9198–9208.
51 A. O. Lykhin and S. A. Varganov, *Phys. Chem. Chem. Phys.*, 2020, **22**, 5500–5508.
52 G. A. Zalesskaya, D. L. Yakovlev, E. G. Sambor and N. N. Bely, *Phys. Chem. Chem. Phys.*, 2002, **4**, 5634–5639.
53 Y. Ide and T. Hikida, *Chem. Phys.*, 1995, **194**, 159–166.
54 K. Artmann, C. H. Pollok, C. Merten and P. Nuernberger, *Phys. Chem. Chem. Phys.*, 2022, **24**, 30017–30026.
55 X. Niu, Z. Kuang, M. Planells, Y. Guo, N. Robertson and A. Xia, *Phys. Chem. Chem. Phys.*, 2020, **22**, 15743–15750.
56 Z. Kuang, G. He, H. Song, X. Wang, Z. Hu, H. Sun, Y. Wan, Q. Guo and A. Xia, *J. Phys. Chem. C*, 2018, **122**, 3727–3737.
57 Y. Wang, Z. Guo, Y. Gao, Y. Tian, Y. Deng, X. Ma and W. Yang, *J. Phys. Chem. Lett.*, 2022, **13**, 6664–6673.
58 Y. Wang, Y. Tian, Y. Gao, Z. Guo, Z. Xue, Y. Han, W. Yang and X. Ma, *J. Phys. Chem. Lett.*, 2023, **14**, 9665–9676.
59 A. Barak, N. Dhiman, F. Sturm, F. Rauch, Y. A. Lakshmanna, K. S. Findlay, A. Beeby, T. B. Marder and S. Umapathy, *ChemPhotoChem*, 2022, **6**, e202200146.
60 A. Barak, N. Dhiman, F. Sturm, F. Rauch, Y. A. Lakshmanna, K. S. Findlay, A. Beeby, T. B. Marder and S. Umapathy, *J. Phys. Chem. C*, 2023, **127**, 5855–5865.
61 W. Zhang, H. Song, J. Kong, Z. Kuang, M. Li, Q. Guo, C. Chen and A. Xia, *J. Phys. Chem. C*, 2019, **123**, 19322–19332.
62 Y. Gao, Y. Wang, Z. Guo, Y. Wan, C. Li, B. Yang, W. Yang and X. Ma, *J. Phys. Chem. B*, 2022, **126**, 2729–2739.
63 Y. Gao, Y. Wang, Z. Guo, Y. Wan, Z. Xue, Y. Han, W. Yang and X. Ma, *Chem. Sci.*, 2024, **15**, 6410–6420.
64 Y. Lee, R. M. Malamakal, D. M. Chenoweth and J. M. Anna, *J. Phys. Chem. Lett.*, 2020, **11**, 877–884.
65 I. E. Serdiuk, M. Mońka, K. Kozakiewicz, B. Liberek, P. Bojarski and S. Y. Park, *J. Phys. Chem. B*, 2021, **125**, 2696–2706.
66 M. Mońka, I. E. Serdiuk, K. Kozakiewicz, E. Hoffman, J. Szumilas, A. Kubicki, S. Y. Park and P. Bojarski, *J. Mater. Chem. C*, 2022, **10**, 7925–7934.
67 R. Schira and C. Latouche, *Dalton Trans.*, 2021, **50**, 746–753.
68 Y. Guo, L. Zhang and Z. Qu, *Molecules*, 2023, **28**, 3257.
69 J.-P. Malrieu and G. Trinquier, *J. Chem. Phys.*, 2016, **144**, 211101.
70 C. M. Marian, *Annu. Rev. Phys. Chem.*, 2021, **72**, 617–640.
71 C. M. Marian, *Wiley Interdiscip. Rev.: Comput. Mol. Sci.*, 2012, **2**, 187–203.
72 K. Božinović, D. Nestić, E. Michail, M. Ferger, M. Košćak, C. Lambert, D. Majhen, T. B. Marder and I. Piantanida, *J. Photochem. Photobiol., B*, 2022, **234**, 112523.
73 M. Ferger, C. Roger, E. Köster, F. Rauch, S. Lorenzen, I. Krummenacher, A. Friedrich, M. Košćak, D. Nestić, H. Braunschweig, C. Lambert, I. Piantanida and T. B. Marder, *Chem.–Eur. J.*, 2022, **28**, e202201130.
74 M. Bregnhøj, F. Thorning and P. R. Ogilby, *Chem. Rev.*, 2024, DOI: **10.1021/acs.chemrev.4c00105**.
75 M. Westberg, L. Holmegaard, F. M. Pimenta, M. Etzerodt and P. R. Ogilby, *J. Am. Chem. Soc.*, 2015, **137**, 1632–1642.
76 M. Bregnhøj, M. Prete, V. Turkovic, A. U. Petersen, M. B. Nielsen, M. Madsen and P. R. Ogilby, *Methods Appl. Fluoresc.*, 2019, **8**, 014001.
77 R. Schmidt, C. Tanielian, R. Dunsbach and C. Wolff, *J. Photochem. Photobiol., A*, 1994, **79**, 11–17.
78 C. Martí, O. Jürgens, O. Cuenca, M. Casals and S. Nonell, *J. Photochem. Photobiol., A*, 1996, **97**, 11–18.
79 F. Wilkinson, W. P. Helman and A. B. Ross, *J. Phys. Chem. Ref. Data*, 1993, **22**, 113–262.
80 C. Schweitzer and R. Schmidt, *Chem. Rev.*, 2003, **103**, 1685–1758.
81 P. R. Ogilby, *Chem. Soc. Rev.*, 2010, **39**, 3181–3209.
82 R. Battino, T. R. Rettich and T. Tominaga, *J. Phys. Chem. Ref. Data*, 1983, **12**, 163–178.